INTRODUCTION

We present a fast multipole-accelerated indirect boundary element method (FMIBEM) for the Helmholtz equation. In [1, 2], we demonstrated a fast multiple-accelerated direct BEM (FMBEM). The direct BEM is applicable only to geometries with closed surfaces. For many cases, this is not a limiting factor: it can handle spheres, boxes, and even human bodies. In fact, in [3], the FMBEM was used to calculate head-related transfer functions for human heads. Other geometries, however, such as very thin objects (e.g., a disk, a piece of glass, etc), can be modeled as closed surfaces, but would require a very large number of elements to do so accurately. The indirect BEM alleviates this issue by modeling such geometries using a formulation based on jump conditions and double-sided elements [4, 5, 6]. The indirect BEM is also convenient for modeling multi-material transmission problems, e.g., for modeling how sound penetrates through a wall made of concrete [5]. To accomplish this task using a direct BEM, the internal and external problems must be modeled separately and linked together later on.

The introduction of double-sided elements in the problem leads to many issues. First, calculating the potential due to an infinitely thin, double-sided element requires computing several singular and hypersingular integrals, which can be difficult to do. Second, the linear system that arises after discretizing the problem is dense, and therefore requires $\mathrm{O}\left(N^2\right)$ storage, where N is the number of elements. For large N, this could limit the size of a problem; for example, a computer with only 8 GB is limited to problems with fewer than 30000 elements. This problem can be avoided by not explicitly storing the matrix coefficients and recomputing them from scratch whenever necessary; however, this method can be more computationally expensive. Solving the system by direct means (e.g., via an LU decomposition) is a $\mathrm{O}\left(N^3\right)$ operation. Using an iterative solver, such as GMRES, can alleviate this issue somewhat, providing a $\mathrm{O}\left(N_{\mathrm{iter}}N^2\right)$ method, where N_{iter} is the number of iterations required. Still for large N, both of these methods can be very slow. Third, non-trivial analytical solutions are needed to validate the numerical solutions; however, there are very few problems for which an analytical solution can be easily constructed.

We make three contributions. First, we have developed a novel strategy for evaluating analytically the singular and hypersingular integrals. Second, we have accelerated the matrix-vector product used by the iterative solver by separating the matrix into two pieces, one for local summations and one for far-field summations. Further, the far-field summations are accelerated using the fast multipole method. The combination of these leads to an iterative solver that runs in $\mathrm{O}(N_{\mathrm{iter}}N)$. Third, we have constructed an analytical solutions for a plane wave scattering off a sound-hard disk. The analytical solution is used to verify the indirect BEM solution. Results from an implementation that incorporates these contributions are discussed.

PROBLEM FORMULATION

Consider a surface, S, on which a discontinuity of the potential and/or its normal derivative may take place. The normal, $\mathbf{n}$, to the surface is directed from side "-" to side "+". Furthermore, we mark paramaters on the surface with superscripts "$\pm$" depending on the side; in particular, $\mathbf{n}^{\pm} = \mp\mathbf{n}$ are the surface normals on the "+" and "-" sides. Let $\phi(\mathbf{y})$ be a radiating function (acoustic pressure or velocity potential), which satisfies the Helmholtz equation outside the surface, S, and can be represented as a sum of single- and double-layer potentials of strengths, $\sigma(\mathbf{x})$ and $\mu(\mathbf{x})$, respectively.

$$\phi(\mathbf{y}) = L[\sigma](\mathbf{y}) + M[\mu](\mathbf{y}) \tag{1}$$

$$\begin{aligned} L[\sigma](\mathbf{y}) &= \int_S \sigma(\mathbf{x}) G(\mathbf{x},\mathbf{y})\, dS(\mathbf{x}), \quad G(\mathbf{x},\mathbf{y}) = \frac{e^{ik|\mathbf{x}-\mathbf{y}|}}{4\pi|\mathbf{x}-\mathbf{y}|} \\ M[\mu](\mathbf{y}) &= \int_S \mu(\mathbf{x}) \frac{\partial G(\mathbf{x},\mathbf{y})}{\partial n(\mathbf{x})} dS(\mathbf{x}) \end{aligned} \tag{2}$$

where k is the wavenumber and $G(\mathbf{x},\mathbf{y})$ is the free-space Green's function. The functions, $\sigma(\mathbf{x})$ and $\mu(\mathbf{x})$, may be determined as soon as proper boundary conditions are specified on S. We assume the following generic

boundary conditions.

$$\begin{aligned} \alpha_1^+\phi^+ + \beta_1^+ q^+ + \alpha_1^-\phi^- + \beta_1^- q^- &= \gamma_1, \\ \alpha_2^+\phi^+ + \beta_2^+ q^+ + \alpha_2^-\phi^- + \beta_2^- q^- &= \gamma_2, \end{aligned} \tag{3}$$

where α, β, and γ are given functions of $\mathbf{x} \in S$ and

$$q^\pm = \frac{\partial \phi^\pm}{\partial n^\pm} = \mathbf{n}^\pm \cdot \nabla \phi^\pm. \tag{4}$$

This form of the boundary conditions includes velocity and pressure conditions provided on each side, pressure and velocity differences across the surface, and various linear combinations of these conditions, and covers all cases encountered in practice. The quantities, α, β, and γ, can not be specified completely arbitrarily, e.g., they should be chosen so that the two conditions in Eq. (3) are linearly independent. We assume that conditions are such that the solution of the problem exists and is unique.

Jump Conditions

Jump conditions provide links between the strengths of the single- and double-layer potentials and $\phi^\pm$ and $q^\pm$. In addition to operators L and M, Eq. (2), we introduce

$$L'[\sigma](\mathbf{y}) = \int_S \sigma(\mathbf{x}) \frac{\partial G(\mathbf{x},\mathbf{y})}{\partial n(\mathbf{y})} dS(\mathbf{x}), \quad M'[\mu](\mathbf{y}) = \frac{\partial}{\partial n(\mathbf{y})} \int_S \mu(\mathbf{x}) \frac{\partial G(\mathbf{x},\mathbf{y})}{\partial n(\mathbf{x})} dS(\mathbf{x}), \tag{5}$$

so that the jump conditions can be written in the form

$$\begin{aligned} \phi^\pm(\mathbf{y}) &= L[\sigma](\mathbf{y}) + M[\mu](\mathbf{y}) \pm \frac{1}{2}\mu(\mathbf{y}), \quad \mathbf{y} \in S, \\ q^\pm(\mathbf{y}) &= \mp\{L'[\sigma](\mathbf{y}) + M'[\mu](\mathbf{y})\} + \frac{1}{2}\sigma(\mathbf{y}), \quad \mathbf{y} \in S. \end{aligned} \tag{6}$$

Substitution of Eqs (6) into boundary conditions (3) results in the following coupled boundary integral equations (BIE) for σ and μ:

$$\begin{aligned} a_1\left(L[\sigma] + M[\mu]\right) + b_1\left(L'[\sigma] + M'[\mu]\right) + c_1\sigma + d_1\mu &= \gamma_1, \\ a_2\left(L[\sigma] + M[\mu]\right) + b_2\left(L'[\sigma] + M'[\mu]\right) + c_2\sigma + d_2\mu &= \gamma_2, \end{aligned} \tag{7}$$

where

$$a_j = \alpha_j^+ + \alpha_j^-, \quad b_j = \beta_j^- - \beta_j^+, \quad c_j = \frac{1}{2}\left(\beta_j^+ + \beta_j^-\right), \quad d_j = \frac{1}{2}\left(\alpha_j^+ - \alpha_j^-\right), \quad j = 1,2. \tag{8}$$

While these BIE could be solved numerically via usual discretization of the boundary integral operator, we will provide an alternative BIE, which is preferable for numerical solution.

Boundary Integral Equations

Let us decompose $\phi^\pm$ and $q^\pm$ as

$$\phi^\pm = u^\pm - b^\pm, \quad q^\pm = u'^\pm - b'^\pm, \tag{9}$$

where $u^\pm$ and $u'^\pm$ are some new unknowns, while $b^\pm$ and $b'^\pm$ can be found from α, β, and γ. In this case jump conditions provide

$$\mu = u^+ - u^- - \left(b^+ - b^-\right), \quad \sigma = u'^+ + u'^- - \left(b'^+ + b'^-\right), \tag{10}$$

and

$$\begin{aligned} \frac{1}{2}\left(u^+ + u^-\right) - L\left[u'^+ + u'^-\right] - M\left[u^+ - u^-\right] &= \frac{1}{2}\left(b^+ + b^-\right) - L\left[b'^+ + b'^-\right] - M\left[b^+ - b^-\right], \\ \frac{1}{2}\left(u'^+ - u'^-\right) + L'\left[u'^+ + u'^-\right] + M'\left[u^+ - u^-\right] &= \frac{1}{2}\left(b'^+ - b'^-\right) + L'\left[b'^+ + b'^-\right] + M'\left[b^+ - b^-\right], \end{aligned} \tag{11}$$

or

$$A[\chi] = c, \tag{12}$$

where A is the system matrix, χ is the vector of nodal variables on both surface sides, $\chi = (\chi^+, \chi^-)'$, $\chi^\pm = \chi^\pm(u^\pm, u'^\pm)$, and c is the right hand side.

Substituting (9) into the boundary conditions (3), we obtain

$$\alpha_j^+ u^+ + \beta_j^+ u'^+ + \alpha_j^- u^- + \beta_j^- u'^- = \gamma_j + \left(\alpha_j^+ b^+ + \beta_j^+ b'^+ + \alpha_j^- b^- + \beta_j^- b'^-\right), \quad j = 1,2. \tag{13}$$

Selection of $b^\pm$ and $b'^\pm$ depends on coefficients α, β, and γ and can be chosen to provide simple non-degenerate forms. For example, if the Neumann boundary conditions are provided on both sides of the surface, i.e.

$$\alpha_{1,2}^\pm = 0, \quad \beta_1^+ = \beta_2^- = 1, \quad \beta_1^- = \beta_2^+ = 0, \tag{14}$$

we can simply set

$$\chi^\pm = u^\pm = \phi^\pm, \quad u'^\pm = 0, \quad b^\pm = 0, \quad b'^+ = -\gamma_1^+, \quad b'^- = -\gamma_2^-, \tag{15}$$

to obtain

$$A[\chi] = \begin{pmatrix} \frac{1}{2}(\chi^+ + \chi^-) - M[\chi^+ - \chi^-] \\ M'[\chi^+ - \chi^-] \end{pmatrix}, \quad c = \begin{pmatrix} L[\gamma_1^+ + \gamma_2^-] \\ -\frac{1}{2}(\gamma_1^+ - \gamma_2^-) - L'[\gamma_1^+ + \gamma_2^-] \end{pmatrix}. \tag{16}$$

Boundary Element Method

The system of integral equations can be discretized using, e.g. center panel collocation method:

$$\begin{aligned} L[\sigma]\left(\mathbf{x}_l^{(c)}\right) &= \sum_{l'=1}^{N} \int_{S_{l'}} \sigma(\mathbf{x}) G\left(\mathbf{x}, \mathbf{x}_l^{(c)}\right) dS(\mathbf{x}) \approx \sum_{l'=1}^{N} L_{ll'} \sigma_{l'}, \\ \sigma_{l'} &= \sigma\left(\mathbf{x}_{l'}^{(c)}\right), \quad L_{ll'} = \int_{S_{l'}} G\left(\mathbf{x}, \mathbf{x}_l^{(c)}\right) dS(\mathbf{x}), \end{aligned} \tag{17}$$

where $\mathbf{x}_l^{(c)}$ is the center of the lth surface element S_l (similar discretizations can be written for operators L', M, and M'). Matrix $\{L_{ll'}\}$ describes effect of element l' on element l and for elements separated by a suffcient cutoff distance r_c, the principal term of the far field expansion of the integral can be used efficiently:

$$L_{ll'} \approx s_{l'} G\left(\mathbf{x}_{l'}^{(c)}, \mathbf{x}_l^{(c)}\right), \quad \left|\mathbf{x} - \mathbf{x}_l^{(c)}\right| > r_c. \tag{18}$$

For close elements or diagonal element computation, we must evaluate nearly singular, singular, or hypersingular integrals, which is usually done numerically, via the use of appropriate quadratures. Also, there are some tricks for reduction of hypersingular integrals to singular integrals [5], which, however, presume that either the surface is closed, or there are appropriate boundary conditions on the edges of the surface, which turn the principal term of hypersingularity to zero. When using such reduction method, care should be provided for boundaries which have discontinuities (angles), free edges, and different types of joints (e.g. T-joints). Direct stable numerical computation of nearly singular and hypersingular integrals can be expensive if using subdivision or similar scheme.

So we propose to treat these integrals completely analytically, which avoids all numerical issues mentioned above. To our best knowledge, expressions derived in the following section are new.

Flat-Panel Integrals

The integrals we consider can be used not only for collocation of the boundary points but also for computation of function (1) and its gradient. So for a flat polygonal element S with vertices $(\mathbf{x}_1, \mathbf{x}_2, .., \mathbf{x}_n)$ which define contour C in plane P with normal $\mathbf{n}$ (see Fig. 1) we need to compute integrals

$$\begin{aligned} L(\mathbf{y}) &= \int_S G(\mathbf{x}, \mathbf{y}) dS(\mathbf{x}), \quad M(\mathbf{y}) = \int_S \mathbf{n} \cdot \nabla_{\mathbf{x}} G(\mathbf{x}, \mathbf{y}) dS(\mathbf{x}), \\ \mathbf{L}'(\mathbf{y}) &= \nabla_{\mathbf{y}} \int_S G(\mathbf{x}, \mathbf{y}) dS(\mathbf{x}), \quad \mathbf{M}'(\mathbf{y}) = \nabla_{\mathbf{y}} \int_S \mathbf{n} \cdot \nabla_{\mathbf{x}} G(\mathbf{x}, \mathbf{y}) dS(\mathbf{x}). \end{aligned} \tag{19}$$

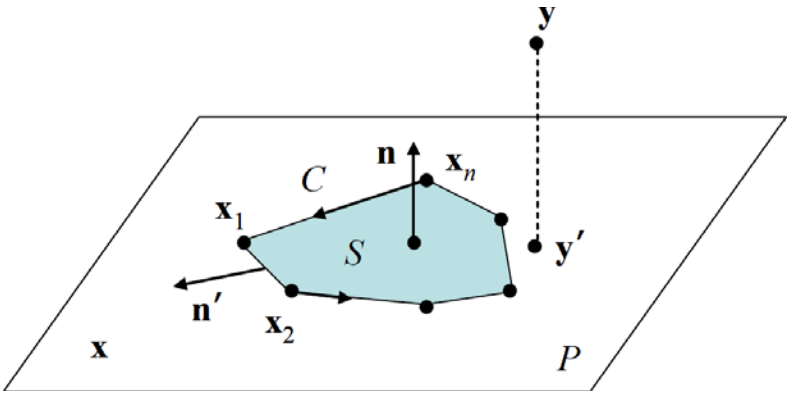

FIGURE 1: The notation used when performing the flat-panel integrals.

The method, which we use is reduction of the surface integral to contour, or line, integrals is based on the two-dimensional Gauss (divergence) theorem. Let $\widetilde{\nabla}$ be a two-dimensional nabla operator acting in plane P:

$$\widetilde{\nabla} = \mathbf{i}_1 \frac{\partial}{\partial x_1} + \mathbf{i}_2 \frac{\partial}{\partial x_2}, \tag{20}$$

where $\mathbf{i}_1$ and $\mathbf{i}_2$ are orthonormal vectors defining Cartesian coordnates (x_1, x_2) in P. The Gauss theorem states

$$L = \int_S \widetilde{\nabla}_{\mathbf{x}} \cdot \mathbf{F}(\mathbf{x}) dS(\mathbf{x}) = \int_C \mathbf{n}'(\mathbf{x}) \cdot \mathbf{F}(\mathbf{x}) dl(\mathbf{x}) = \sum_{j=1}^{n} \int_{C_j} \mathbf{n}'(\mathbf{x}) \cdot \mathbf{F}(\mathbf{x}) dl(\mathbf{x}), \quad \widetilde{\nabla}_{\mathbf{x}} \cdot \mathbf{F}(\mathbf{x}) = G(\mathbf{x}, \mathbf{y}), \tag{21}$$

where $\mathbf{F}(\mathbf{x})$ is a differentiable function everywhwere in S and $\mathbf{n}'(\mathbf{x})$ is the outer normal to C (for right-hand orientation, which we assume here and everywhere below, see Fig. 1). As we consider polygons, i.e. contours with corners at which the normal is not defined, we break the contour into smooth pieces $l_1, ..., l_n$ (edges of the polygon) and perform integration for each piece separately. By choosing $\mathbf{F}(\mathbf{x})$ in the form

$$\begin{aligned} \mathbf{F}(\mathbf{x}) &= \rho f(\rho; h), \quad f(\rho; h) = \frac{e^{ikr} - e^{ik|h|}}{4\pi i k \rho^2}, \\ \mathbf{y} &= \mathbf{n}h + \mathbf{y}', \quad |\mathbf{x} - \mathbf{y}| = r = \sqrt{\rho^2 + h^2}, \quad \rho = \mathbf{x} - \mathbf{y}' \in P, \quad \rho = |\rho|, \end{aligned} \tag{22}$$

we obtain for elementary contour integrals

$$I_j(x', y', z') = \int_{C_j} \mathbf{n}'(\mathbf{x}) \cdot \mathbf{F}(\mathbf{r}) dl(\mathbf{x}) = H(l_j - x', y', z') - H(-x', y', z'), \tag{23}$$

where the primitives

$$H(x, y', z') = -z' \int f(\rho; y') dx = \frac{-z'}{4\pi i k} \int \frac{e^{ikr} - e^{iky'}}{x^2 + z'^2} dx, \quad r = \sqrt{x^2 + y'^2 + z'^2}, \tag{24}$$

where f is given by Eq. (22).

We developed a fast recursive method to compute these primitives with an arbitrary accuracy based on expansions over small parameter $\epsilon = k|\mathbf{x} - \mathbf{x}_j|/\pi \ll 1$, which is a ratio of the element size to the wavelength. These expansions converge fast and deliver analytical quality solution, which also can be differentiated to obtain integrals $M, \mathbf{L}'$, and $\mathbf{M}'$ in Eq. (19). Details of the method will be presented in a follow-up paper.

USE OF THE FAST MULTIPOLE METHOD

The FMM strategy for boundary element methods was discussed in [2]. According to [2], the discretization should be selected in a way that approximation of far field integrals (18) is good enough. The

space partitioning with octree should be designed in a way that the size of the smallest box δ is larger than the cutoff distance, $\delta > r_c$. In this computation of matrix entries corresponding to the interactions between closely located elements can be done using analytical formulae, while far field interactions are obtained via regular FMM procedures involving multipole and local expansions and translations.

The FMM for the Helmholtz kernel used here is the same as in [2]. Relatively small modifications related to stabilization of translation procedures were made, which enabled computations for wider range of parameter kD, where D is the size of the computational domain (diagonal of the bounding cube) (up to $kD \sim 10^3$, which is determined by the memory size and reasonable computation time on the workstation used). Higher accuracy FMM was used in the outer loop of the iteration process realized via the fGMRES, while lower accuracy FMM was used for preconditioning in the inner fGMRES loop as described in [2].

NUMERICAL EXAMPLES

The FMIBEM was implemented in FORTRAN 95 using OpenMP parallelization, which brings substantial speedups on multicore PCs. The results seen below for the scattering off a sphere were collected using a four-core PC (Intel Core 2 Extreme QX6700 at 2.66 GHz) with 8GB of RAM, for which overall parallelization efficiency was close to 100%. The results seen below for the scattering off a disk were collected using a eight-core PC (Intel Xeon X5560 CPU at 2.8 GHz) with 24 GB of RAM. We report only some details of studies of scattering off a sphere and a disk, while tests for other geometries, including scattering off disks with ripples, multiple closed and open objects, and shapes or biological objects were also performed. Acoustic fields generated by vibrating boxes with openings and T-junctions were also computed. In addition we did some tests with the direct BEM described in [2], which we used in the settings diescribed in the reference and with analytical formulae for the boundary integrals described in the present paper. In the latter case the analytical formulae were applied for elements which centers were closer that the cutoff distance r_c.

Scattering off a Sphere

The FMIBEM can be used for closed-surface computations. The case of scattering off a sphere is attractive for tests, due to analytical solution is available for the plane wave incident field $\phi^{in}(\mathbf{r}) = e^{ik\mathbf{s}\cdot\mathbf{r}}$, $\mathbf{s} = \mathbf{k}/k$, where $\mathbf{k}$ is the wave vector (e.g. see [1, 7])

$$\phi^{tot}\big|_S(\mathbf{s}') = \frac{i}{(ka)^2}\sum_{n=0}^{\infty}\frac{(2n+1)i^n P_n(\mathbf{s}\cdot\mathbf{s}')}{h_n'(ka)+(i\sigma_b/k)h_n(ka)}, \quad \left.\frac{\partial\phi^{tot}}{\partial n}+i\sigma_b\phi^{tot}\right|_S = 0, \quad \phi^{tot} = \phi^{in}+\phi^{scat}, \tag{25}$$

where a is the sphere radius, $\mathbf{s}'$ is a unit vector pointing to the evaluation surface point, σ_b is the boundary admittance (zero for sound hard and infinity for sound-soft surfaces), P_n and h_n are the Legendre polynomial and the spherical Hankel function of the first kind of order n, while ϕ^{tot} and ϕ^{scat} are the total and scattered fields. So the error of the solution can be measured with respect to the analytical solution.

There are several sources of the error, namely: 1) geometrical errors due to flat panel surface discretization; 2) errors due to the center panel collocation scheme accepted; 3) errors due to computation of integrals using constant panel approximation; 4) errors due to truncation of series in computation of the boundary integrals; 5) errors of the far-field approximation (needed for efficient FMM); 6) errors of the FMM due to approximate character of matrix-vector multiplication; 7) terminal iteration error, since the linear system was solved using iterative scheme. Some of these errors are easily controllable, while some of them are intrinsic for the method used, depend on the configurations and may show a slow decay (e.g. geometrical errors as functions of the number of boundary elements). In tests we set errors 4), 6) and 7) all to level 10^{-4}. We also used as default the cut-off radius for far field approximations $r_c = 2d_{\max}$, where $d_{\max}$ is the maximum diameter of the element in the mesh. It was found that this value is good enough in terms of acuracy and performance, while for meshes with large number of elements $N \gtrsim 10^5$ it was found that increase of r_c to $3d_{\max}$ or so is required to provide the same level of errors. The meshes used sampled the surface with at least 6 elements per wave length. Typical errors in the BEM solutions measured in absolute L_∞ and relative L_2 norms were of the order 1%, which we consider as usual for other version of the boundary

element methods (in many cases these errors could be reduced by orders of magnitude but for a substantial computational cost).

Table 1 provides some data on speed and memory usage for different options. In these runs, the wavenumber and mesh size were changed to maintain $kd_{\max} = 2\pi/6$ (i.e., six maximum size surface elements per wavelength). Subscripts 1, 2, and 3 correspond to the speed and memory usage options described above. Some data in this table is missing because of either excessive computational time (option 1) or excessive memory request (option 3). In the table times are given as total wall clock times to perform the entire algorithm, and memory is shown as a peak of the requested memory.

TABLE 1: Running times and memory usage for different mesh sizes and values of kD.

N	kD	t_1 (s)	t_2 (s)	t_3 (s)	mem_1 (GB)	mem_2 (GB)	mem_3 (GB)
50700	83.4	1.29×10^3	354	193	0.31	1.00	5.22
101568	118	3.19×10^3	592	411	0.62	1.95	5.58
202800	167	2.06×10^4	4.59×10^3	N/A	1.02	3.54	N/A
401868	235	N/A	4.59×10^3	N/A	N/A	7.12	N/A

It is seen that option 2 somehow compromise between the two extreeme cases and enables computations for meshes up to $\sim 5 \cdot 10^5$ on the PC used. Of course, the algorithm can be executed on different workstations/clusters where the fastest option can be realized for broader range of N. It is seen that for options 1 and 2, the memory required is scaled approximately linearly with N. On the other hand, for option 3, the memory depends not on the number of computed integrals, but on the number of points in the boxes at the finest level of the FMM octree. This changes discretely as depth of the octree changes. For example, for the case of $N \approx 2 \times 10^5$, there was not enough memory to execute the fastest option. The total execution time also changes non-uniformly due to many factors. For example, for option 2, the computational times appeared to be the same for cases $N \approx 2 \times 10^5$ and $N \approx 4 \times 10^5$. However more detailed analysis of this case shows that, in fact the time for the matrix-vector product in the outer loop increased approximately 2 times (from about 16 s to 36 s), while by some reasons (e.g. proximity to the spurious modes can play a role) the number of iterations decreased from 39 to 30 and the total number of cycles in the inner fGMRES loop (preconditioning) reduced from 418 to 319 (the time for the matrix-vector product in the inner loop increased from 9.3 s to 10.5 s). Based on this analysis we can see, that computation of high kD cases for the present algorithm is limited by computational memory requirements (or high execution time). This does not prevent use of the FMM for evaluation of the solution at field points, for which kD can be much larger (no storage for one matrix-vector product is required).

Scattering off a Disk

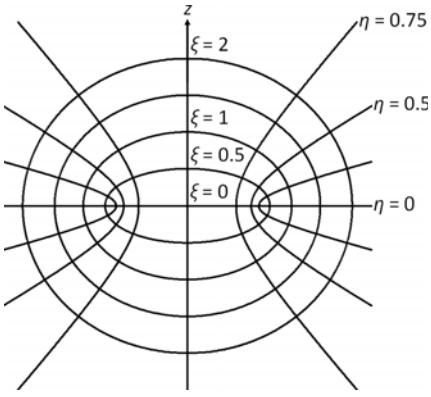

FIGURE 2: The oblate spheroidal coordinate system. A disk can be represented by the surface, $\xi = 0$.

An analytical problem for the validation of the indirect BEM for the case of scattering off a non-closed surface was not readily available to us. We accordingly developed one – the scattering off a disk. Consider a

sound-hard disk of radius, a, centered at the origin and perpendicular to the z axis. We wish to calculate an analytical expression for the scattered potential resulting from a plane wave striking the disk from directly above, $\phi^{\text{in}} = \exp(-ikz)$. To calculate the scattered potential, ϕ^{scat}, note that a disk can be represented as an oblate spheroid that has been squashed down to a thickness of zero. Figure 2 shows the oblate spheroidal coordinate system, which can be constructed by rotating the two-dimensional elliptical coordinate system around the minor axis. The Helmholtz equation can be written in oblate spheroidal coordinates as [8, 9]

$$\left(\frac{\partial}{\partial\eta}\left(1-\eta^2\right)\frac{\partial}{\partial\eta}+\frac{\partial}{\partial\xi}\left(\xi^2+1\right)\frac{\partial}{\partial\xi}+\frac{\eta^2+\xi^2}{\left(1-\eta^2\right)\left(\xi^2+1\right)}\frac{\partial^2}{\partial\varphi^2}+c^2\left(\eta^2+\xi^2\right)\right)\phi=0 \tag{26}$$

After applying the method of separation of variables, any solution to the Helmholtz equation in oblate spheroidal coordinates can be written as [8]

$$\phi=\sum_{m=0}^{\infty}\sum_{n=m}^{\infty}S_{mn}\left(-ic,\eta\right)\left(A_{mn}R_{mn}^{(1)}\left(-ic,i\xi\right)+B_{mn}R_{mn}^{(3)}\left(-ic,i\xi\right)\right)\exp\left(im\varphi\right) \tag{27}$$

where A_{mn} and B_{mn} are expansion coefficients dependent on the problem at hand, $S_{mn}\left(-ic,\eta\right)$ is the oblate spheroidal angle function, and $R_{mn}^{(1)}\left(-ic,i\xi\right)$ and $R_{mn}^{(3)}\left(-ic,i\xi\right)$ are the oblate spheroidal radial function of the first and third kinds, respectively. For the problem at hand [7],

$$\phi^{\text{scat}}=-2\sum_{n=0}^{\infty}\frac{i^n}{N_{0n}}S_{0n}\left(-ic,-1\right)\frac{R_{0n}^{(1)\prime}\left(-ic,i0\right)}{R_{0n}^{(3)\prime}\left(-ic,i0\right)}S_{0n}\left(-ic,\eta\right)R_{0n}^{(3)}\left(-ic,i\xi\right) \tag{28}$$

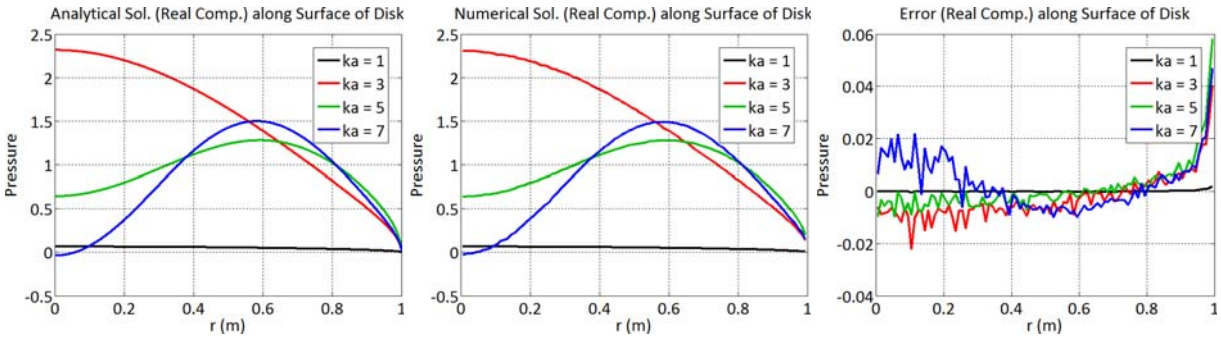

FIGURE 3: The real component of the analytical solution (on the left) and the numerical solution (in the middle) along the top surface of the disk for different values of ka. The mesh size used for the numerical solution in this example was 62732. On the right is a plot of the error of the numerical solution.

Figure 3 shows the real component of the analytical and numerical solutions along the top surface of the disk for different values of ka, as well as the error of the numerical solution. Figure 4 show the running time and error of the FMIBEM as a function of mesh size for different values of ka. The running time is nearly linear, and the error decays to below 1% quite quickly. For these simulations, we chose $r_c = 7d_{\max}$ to prevent error at larger mesh sizes.

CONCLUSION

This paper described a fast-multipole accelerated indirect BEM. The indirect BEM provides a convenient and accurate method for modeling very thin surfaces or interfaces between different materials. The indirect BEM accomplishes this by using double-sided elements. This paper made several contributions: (1) providing analytical expressions for the singular and hypersingular integrals arising from the double-sided elements; (2) using the fast multipole method to decrease the computational cost of the matrix-vector product used in the iterative solver; and (3) comparing the numerical solution for a sound-hard disk to an analytical solution written in terms of oblate spheroidal wave functions. The numerical solutions were very good, containing less than 1% error in most cases. However, in some cases with complex geometries, slow convergence was observed, which shows that more work is needed on efficient preconditioning of the method.

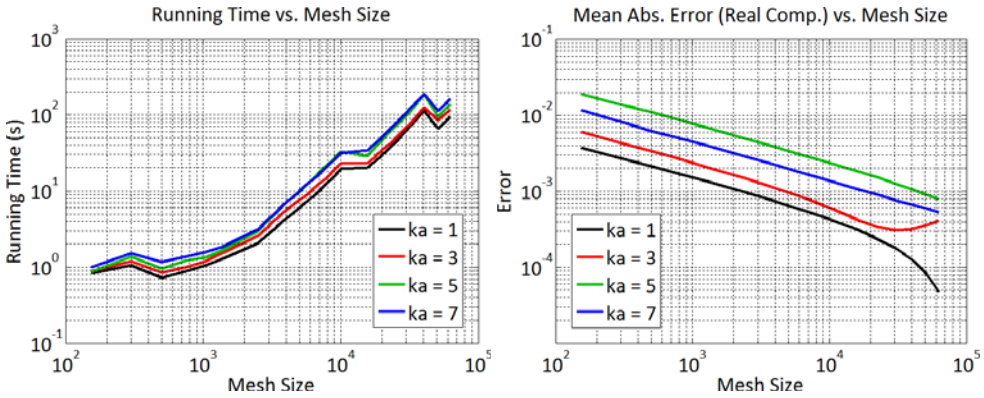

FIGURE 4: On the left: the running time of the FMIBEM for calculating the solution of a disk as a function of mesh size for different values of ka. On the right: the mean absolute error of the real component of the numerical solution when calculated at points in space around the disk as a function of mesh size for different values of ka.

REFERENCES

[1] N. Gumerov and R. Duraiswami, *Fast Multipole Methods for the Helmholtz Equation in Three Dimensions* (Elsevier, Oxford, UK) (2004).

[2] N. Gumerov and R. Duraiswami, "A broadband fast multipole accelerated boundary element method for the three dimensional helmholtz equation", J. Acoust. Soc. Am. **125**, 191–205 (2009).

[3] N. Gumerov, A. O'Donovan, R. Duraiswami, and D. Zotkin, "Computation of the head-related transfer function via the fast multipole accelerated boundary element method and its spherical harmonic representation", J. Acoust. Soc. Am. **127**, 370–386 (2010).

[4] N. Vlahopoulos, "Indirect variational boundary element method in acoustics", In: T.W. Wu (ed) Boundary Element Acoustics: Fundamentals and Computer Codes (Advances in Boundary Elements), Chapter 6, 83–115, WIT Press, Wessex, UK (2000).

[5] S. Raveendra, N. Vlahopoulos, and A. Glaves, "An indirect boundary element formulation for multi-valued impedance simulation in structural acoustics", Applied Mathematical Modeling **22**, 379–393 (1998).

[6] I. Mathews and R. Jeans, "An acoustic boundary integral formulation for open shells allowing different impedance conditions, top and bottom surfaces", J. Sound and Vibration **300**, 580–588 (2007).

[7] J. Bowman, T. Senior, and P. Uslenghi, *Electromagnetic and Acoustic Scattering by Simple Shapes* (Hemisphere Publishing Corporation, New York) (1987).

[8] C. Flammer, *Spheroidal Wave Functions* (Dover Publications, Mineola) (2005).

[9] S. Zhang and J. Jin, *Computation of Special Functions* (Wiley-Interscience) (1996).